



Cite this: *RSC Adv.*, 2017, 7, 50234Received 5th September 2017  
Accepted 21st October 2017

DOI: 10.1039/c7ra09872c

rsc.li/rsc-advances

# Near-infrared optical performances of two Bi<sub>2</sub>Se<sub>3</sub> nanosheets†

Hanhan Xie,<sup>a</sup> Jundong Shao,<sup>b</sup> Jiahong Wang,<sup>\*b</sup> Zhengbo Sun,<sup>b</sup> Xue-Feng Yu <sup>\*b</sup> and Qu-Quan Wang <sup>\*a</sup>

Bi<sub>2</sub>Se<sub>3</sub> has been widely used as a promising photothermal and photoacoustic agent recently. Herein, two-dimensional (2D) Bi<sub>2</sub>Se<sub>3</sub> nanosheets with different sizes of about 30 nm (Bi<sub>2</sub>Se<sub>3</sub>-30) and 80 nm (Bi<sub>2</sub>Se<sub>3</sub>-80) have been successfully synthesized via solution-based methods. Both of the Bi<sub>2</sub>Se<sub>3</sub> nanosheets possess high near-infrared (NIR) optical absorption, efficient photothermal conversion and excellent photoacoustic behaviors. Meanwhile, the Bi<sub>2</sub>Se<sub>3</sub>-30 nanosheets perform better. These results indicate the smaller Bi<sub>2</sub>Se<sub>3</sub> nanosheets are more promising for optical diagnostic and photothermal therapy.

## 1. Introduction

As new quantum matter, topological insulators are one of the most exciting research topics in physics, chemistry and materials fields.<sup>1,2</sup> In recent years, great efforts have been devoted to theoretical prediction and experimental confirmation of various 2D topological insulators such as Bi<sub>2</sub>Se<sub>3</sub>, Bi<sub>2</sub>Te<sub>3</sub>, Sb<sub>2</sub>Te<sub>3</sub> etc.<sup>3–7</sup> Among them, Bi<sub>2</sub>Se<sub>3</sub> invokes a research boom due to its simple band structure near the Dirac point and remarkable band gap.<sup>3–5</sup> The unique band structure of Bi<sub>2</sub>Se<sub>3</sub> lead to new electronic and optical properties.<sup>8,9</sup> For instance, owing to its graphene-like Dirac energy band structure in its surface state, Bi<sub>2</sub>Se<sub>3</sub> can operate as a broadband optical material possess remarkable NIR absorption capacity. Furthermore, Bi<sub>2</sub>Se<sub>3</sub> nanosheets exhibit good bioactivity, biocompatibility, and metabolizability, thus have been proposed as a novel NIR optical nanoagent for bioimaging and therapy applications.<sup>10–13</sup> Their advantageous 2D structure is also promising for many other biomedical applications such as drug delivery.<sup>14</sup>

It is known that the size of the quantum materials is critically important to their chemical, physical and biological properties. For 2D Bi<sub>2</sub>Se<sub>3</sub>, the decrease of diameter or thickness can enlarge the energy gap,<sup>15</sup> enhance the electron-phonon coupling,<sup>16</sup> and regulate the optical properties.<sup>9</sup> On the other hand, the size of Bi<sub>2</sub>Se<sub>3</sub> is also crucial when used as a nanoagent in biomedical applications, which influences not only its cell uptake and biocompatibility,<sup>17</sup> but also its *in vivo* clearance.<sup>18</sup> Recently, many

research groups including ours have established polyol synthesis strategies to prepare Bi<sub>2</sub>Se<sub>3</sub> nanosheets and investigate their optical properties.<sup>13,19–23</sup> However, the size effect on the optical properties of Bi<sub>2</sub>Se<sub>3</sub> nanosheets has not been reported.

In this study, two Bi<sub>2</sub>Se<sub>3</sub> nanosheets with well-controlled particle sizes of 30 nm and 80 nm are synthesized and their optical absorption properties, NIR photothermal and photoacoustic performances are systematically investigated.

## 2. Experimental section

### 2.1. Materials

The materials used in this study, selenium powders (Se, 99.0%), acetone (≥99.8%) and ethylene glycol (EG, ≥99.0%) were obtained from Sinopharm Chemical Reagent Co. Ltd. (Shanghai, China). Sodium borohydride (NaBH<sub>4</sub>, 96.0%), bismuth nitrate pentahydrate (Bi(NO<sub>3</sub>)<sub>3</sub>·5H<sub>2</sub>O, 99.99+%), poly(vinylpyrrolidone) (PVP, MW ≈ 55 000), sodium selenite (Na<sub>2</sub>SeO<sub>3</sub>, 99.0%), and hydroxylamine (NH<sub>2</sub>OH) were purchased from Sigma-Aldrich. Ultrapure water (18.25 MΩ cm, 25 °C) was used in the experiments.

### 2.2. Synthesis of Bi<sub>2</sub>Se<sub>3</sub>-30 nanosheets

The Bi<sub>2</sub>Se<sub>3</sub>-30 nanosheets were synthesized following our previously reported method.<sup>20</sup> Firstly, the sodium hydrogen selenium (NaHSe) solution was pre-produced by the reaction of NaBH<sub>4</sub> aqueous solution and Se powders in an ice-water bath. Then, 0.5 g Bi(NO<sub>3</sub>)<sub>3</sub>·5H<sub>2</sub>O and 0.226 g PVP were mixed at room temperature in ethylene glycol (EG). The well-mixed transparent solution turned turbid yellow when heated to 160 °C under a nitrogen environment. The pre-prepared oxygen-free NaHSe solution (0.667 mol L<sup>-1</sup>, 1.048 mL) was rapidly injected into the mixture by a syringe. The mixture turned dark immediately, indicating the formation of Bi<sub>2</sub>Se<sub>3</sub>-30 nanosheets. The reaction was continued 10 min before cooling to room temperature.

<sup>a</sup>Department of Physics, Key Laboratory of Artificial Micro- and Nano-structures of Ministry of Education, School of Physics and Technology, Wuhan University, Wuhan 430072, China. E-mail: qqwang@whu.edu.cn

<sup>b</sup>Institute of Biomedicine and Biotechnology, Shenzhen Institutes of Advanced Technology, Chinese Academy of Sciences, Shenzhen 518055, P. R. China. E-mail: xf.yu@siat.ac.cn; jh.wang1@siat.ac.cn

† Electronic supplementary information (ESI) available. See DOI: 10.1039/c7ra09872c



### 2.3. Synthesis of Bi<sub>2</sub>Se<sub>3</sub>-80 nanosheets

The Bi<sub>2</sub>Se<sub>3</sub>-80 nanosheets were synthesized as previously published.<sup>19</sup> 1.0 g PVP was dissolved in 50 mL EG, then poured into 250 mL round-bottom flask, followed by the addition of a solution of Na<sub>2</sub>SeO<sub>3</sub> (0.242 g in 35 mL of EG) and Bi(NO<sub>3</sub>)<sub>3</sub>·5H<sub>2</sub>O (0.452 g in 25 mL of EG) under magnetic stirring at room temperature. The sealed flask was heated to 160 °C under a nitrogen environment. The reaction took place by rapid injection of a hydroxylamine solution (NH<sub>2</sub>OH, 2.4 mL in 20 mL of EG). The reaction mixture turned dark purple immediately, indicating the formation of Bi<sub>2</sub>Se<sub>3</sub>-80 nanosheets. The reaction was continued 10 min for a complete reaction before cooling to room temperature.

### 2.4. Characterizations

Transmission electron microscopy (TEM) and high-resolution TEM (HR-TEM) images were acquired on the Tecnai G2 F20 S-Twin transmission electron microscope at an acceleration voltage of 200 kV. Powder X-ray diffraction (XRD) patterns were obtained on the D8 Advance (Bruker, Germany) with Cu K $\alpha$  radiation ( $\lambda = 0.1542$  nm) at 40 kV and 40 mA. Energy-dispersive X-ray spectrometry (EDS) was performed on the SEM equipped with an Oxford INCA 300. Atomic force microscopy (AFM) images were obtained from the MFP-3D-S atomic force microscope (Asylum Research, USA) using the AC mode (tapping mode) in the air. The UV-vis-NIR extinction spectra were recorded on a Lambda25 spectrophotometer (PerkinElmer) with QS-grade quartz cuvettes at room temperature. The Bi<sub>2</sub>Se<sub>3</sub> concentrations were measured by an inductively-coupled plasma optical emission spectrometry (ICP-OES, 7000DV, PerkinElmer).

### 2.5. NIR photothermal effect measurement

The NIR photothermal effect was determined with an infrared thermal imaging camera (Fluke Ti27, USA), using the fiber-coupled continuous semiconductor diode laser (808 nm, KS-810F-8000, Kai Site Electronic Technology Co., Ltd. Shanxi, China) as the irradiation source. All samples were dispersed in ultrapure water with the same absorbance intensities as 0.3 at 808 nm. Subsequently, a 1 cm path length quartz cuvette containing 1 mL of the corresponding sample was irradiated by the laser with a power density of 1.0 W cm<sup>-2</sup> for 12 min. The laser spot was adjusted to cover the entire surface of the sample. The temperature during the heating and cooling periods was recorded one time per 30 s by the infrared thermal imaging camera.

### 2.6. Photoacoustic performance

The Bi<sub>2</sub>Se<sub>3</sub> nanosheets aqueous solutions were placed in a hemispherical acrylic holder and suspended in the center of the imaging dimple of the Endra Nexus 128 photoacoustic instrument. The transducers were coupled to the sample plane by filling the bowl with water and maintained at 38 °C by a pumping system. The photoacoustic signals were obtained at an incident laser wavelength of 808 nm. The photoacoustic signal intensities were acquired by using the ROI in the baseline image and the intensity changes in the ROI of the sample images were calculated.

## 3. Results and discussion

### 3.1. Synthesis and characterizations of Bi<sub>2</sub>Se<sub>3</sub> nanosheets

The two kinds of Bi<sub>2</sub>Se<sub>3</sub> nanosheets were synthesized by solution-based methods illustrated in Experimental section. The morphologies of these Bi<sub>2</sub>Se<sub>3</sub> nanosheets were characterized by TEM and HR-TEM (Fig. 1). The TEM images in Fig. 1a and b reveal the uniform morphologies of these two Bi<sub>2</sub>Se<sub>3</sub> nanosheets. According to the statistical TEM analysis of 200 nanosheets, the average lateral sizes of the two Bi<sub>2</sub>Se<sub>3</sub> nanosheets are determined to be approximately 30  $\pm$  5 nm (denoted as Bi<sub>2</sub>Se<sub>3</sub>-30) and 80  $\pm$  15 nm (denoted as Bi<sub>2</sub>Se<sub>3</sub>-80), respectively. Different from the smooth surface of the Bi<sub>2</sub>Se<sub>3</sub>-30 nanosheets (Fig. 1c), a screw protrusion is observed in the center of the Bi<sub>2</sub>Se<sub>3</sub>-80 nanosheets (Fig. 1e). The morphological differences may be attributed to the supersaturation of the reaction system.<sup>24</sup> However, the lattice fringes in Fig. 1d and f are both ascribed to the (110) plane of Bi<sub>2</sub>Se<sub>3</sub> as 0.21 nm, which suggest similar crystalline structures between the two Bi<sub>2</sub>Se<sub>3</sub> nanosheets.<sup>13</sup> Additionally, the XRD analyses confirm the rhombohedral structure of the two Bi<sub>2</sub>Se<sub>3</sub> nanosheets (JCPDS card no. 33-0214) (Fig. S1†).<sup>25</sup> The chemical compositions of them were further determined by EDS. It is confirmed that their ratios of Bi to Se both are 2 : 3 (Fig. S2†).

The AFM images in Fig. 2 show the 3D topographic morphologies of the Bi<sub>2</sub>Se<sub>3</sub>-30 and Bi<sub>2</sub>Se<sub>3</sub>-80 nanosheets, the corresponding thicknesses are determined by the cross-sectional analysis. The average thickness of the Bi<sub>2</sub>Se<sub>3</sub>-30 nanosheets measured in the AFM image is statistically 1.8  $\pm$  0.5 nm (Fig. 2b), which is as thin as two quintuple atomic layers of Bi<sub>2</sub>Se<sub>3</sub>. Comparatively, the average thickness of the Bi<sub>2</sub>Se<sub>3</sub>-80 nanosheets is 8.3  $\pm$  1.0 nm (Fig. 2d), corresponding to a stack of 8  $\pm$  1 quintuple layers.

### 3.2. Optical absorption properties

The absorption properties of the two Bi<sub>2</sub>Se<sub>3</sub> nanosheets are further investigated. As shown in Fig. 3, the aqueous solution of the two Bi<sub>2</sub>Se<sub>3</sub> nanosheets exhibit obvious absorption ranging

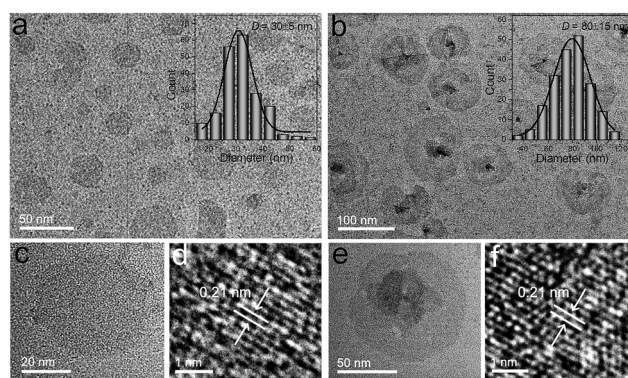


Fig. 1 TEM images of (a) Bi<sub>2</sub>Se<sub>3</sub>-30 and (b) Bi<sub>2</sub>Se<sub>3</sub>-80 nanosheets. Insets: diameter statistical graphs determined from the TEM images; (c) magnified TEM and (d) HR-TEM images of Bi<sub>2</sub>Se<sub>3</sub>-30 nanosheets; (e) magnified TEM and (f) HR-TEM images of Bi<sub>2</sub>Se<sub>3</sub>-80 nanosheets.



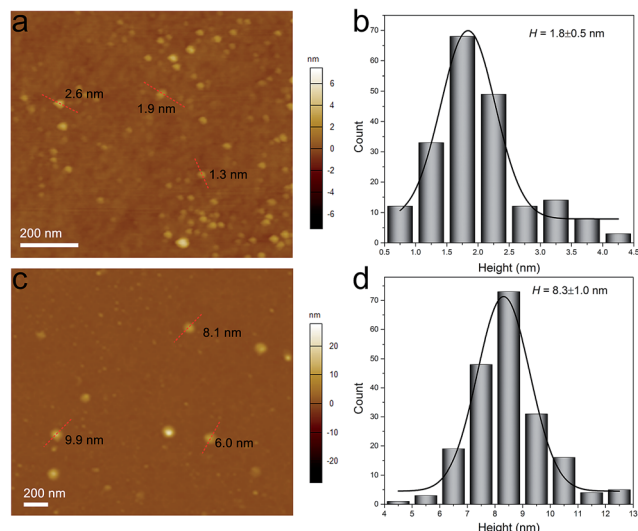


Fig. 2 AFM images and height statistical analysis of (a, b)  $\text{Bi}_2\text{Se}_3$ -30 and (c, d)  $\text{Bi}_2\text{Se}_3$ -80 nanosheets.

from ultraviolet to NIR, which is similar to other 2D layered materials such as graphene oxide<sup>26</sup> and black phosphorus.<sup>27</sup>

Since the nanosheets concentrations ( $C$ ) are measured by ICP-OES, and the extinction intensities against the quartz cell length ( $A/L$ ) at  $\lambda = 808$  nm are determined, the corresponding extinction coefficient  $\epsilon$  can be obtained by using Beer's law:  $A/L = \epsilon C$ . The extinction coefficients of  $\text{Bi}_2\text{Se}_3$ -30 and  $\text{Bi}_2\text{Se}_3$ -80 nanosheets at 808 nm are determined to be 11.3 and 10.7  $\text{L g}^{-1} \text{cm}^{-1}$ , respectively. Both values are noticeably higher than the common photothermal agent gold nanorods (GNRs) ( $3.9 \text{ L g}^{-1} \text{cm}^{-1}$ ).<sup>28</sup>

The optical band gap ( $E_g$ ) of the two  $\text{Bi}_2\text{Se}_3$  nanosheets are also investigated.  $E_g$  can be determined by the equation:  $(\alpha h\nu)^n = B(h\nu - E_g)$ ,<sup>29</sup> in which  $\alpha$  is the absorption coefficient,  $h\nu$  is photon energy, and  $B$  is a constant. Here  $n = 2$  offers the best fit for the optical absorption data of  $\text{Bi}_2\text{Se}_3$ .<sup>29–31</sup> The plots of  $(\alpha h\nu)^2$  versus  $h\nu$  for the  $\text{Bi}_2\text{Se}_3$  nanosheets are shown in Fig. S3.† The  $E_g$  of the two  $\text{Bi}_2\text{Se}_3$  nanosheets are acquired by extrapolating the straight portion of the plot to intersect the energy axis. The  $E_g$  of the  $\text{Bi}_2\text{Se}_3$ -30 and  $\text{Bi}_2\text{Se}_3$ -80 nanosheets are determined to be 2.14 and 1.99 eV, respectively.

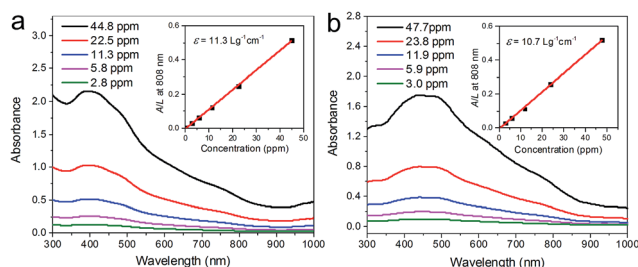


Fig. 3 Absorption spectra of (a)  $\text{Bi}_2\text{Se}_3$ -30 and (b)  $\text{Bi}_2\text{Se}_3$ -80 nanosheets with various concentrations. Insets: absorbance intensities against the quartz cell length ( $A/L$ ) with different concentrations ( $C$ ) at 808 nm.

### 3.3. Photothermal performance

The NIR photothermal performances of the two  $\text{Bi}_2\text{Se}_3$  nanosheets were investigated by dispersing them in water with the same absorbance intensity of 0.30 at 808 nm. Then, the temperatures were measured during the irradiation of an 808 nm laser at low power density ( $1.0 \text{ W cm}^{-2}$ ) for 12 min.

The photographs and corresponding infrared thermal images of the solutions are shown in Fig. 4a, and their temperature heating and cooling curves are shown in Fig. 4b. Compared with pure water, the aqueous solutions of the two  $\text{Bi}_2\text{Se}_3$  nanosheets show much more significant temperature increase. To further uncover the photothermal performance of the two  $\text{Bi}_2\text{Se}_3$  nanosheets, the photothermal conversion efficiency ( $\eta$ ) is calculated based on the energy balance of the system as shown below:<sup>32–34</sup>

$$\eta = (hS(T_{\max} - T_{\text{surr}}) - Q_{\text{dis}})/I(1 - 10^{-A}) \quad (1)$$

$$hS = \sum mC_p/\tau_s \quad (2)$$

Where  $h$  is the heat transfer coefficient,  $S$  is the surface area of the container,  $T_{\max}$  is the maximum temperature at steady-state,  $T_{\text{surr}}$  is the surrounding ambient temperature,  $I$  is the laser power density ( $1.0 \text{ W cm}^{-2}$ ), and  $A$  is the absorption intensity at 808 nm ( $A_{808} = 0.3$ ).  $Q_{\text{dis}}$  is the heat associated with light absorption by the solvent. The variable  $\tau_s$  is the time constant for the heat transfer from the system,  $m$  and  $C_p$  are the mass (1.0 g) and the specific heat capacity ( $4.2 \text{ J g}^{-1} \text{C}^{-1}$ ) of the water used as the solvent. According to eqn (1) and (2), the  $\eta$  values of the  $\text{Bi}_2\text{Se}_3$ -30 and  $\text{Bi}_2\text{Se}_3$ -80 nanosheets are calculated to be 33% and 25%, respectively. The  $\eta$  value of the  $\text{Bi}_2\text{Se}_3$ -30 nanosheets

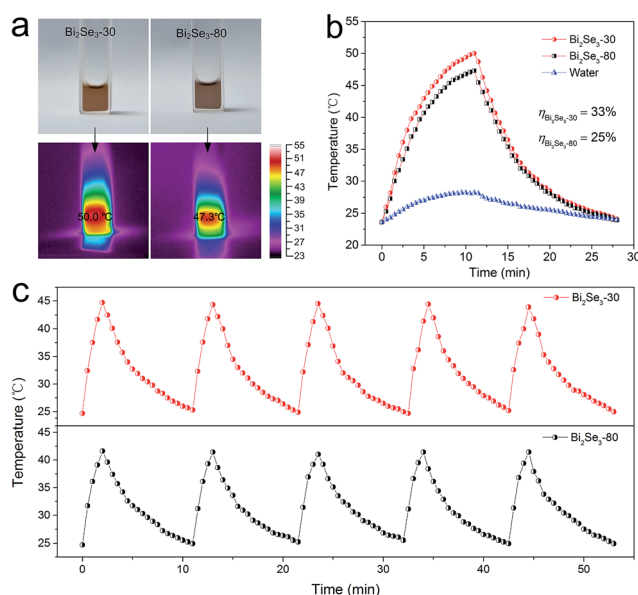


Fig. 4 (a) Photographs (top) and infrared thermal images (down) of the two  $\text{Bi}_2\text{Se}_3$  nanosheets aqueous solution with the same absorption intensities of 0.3 at 808 nm. (b) Photothermal heating/cooling curves of the two  $\text{Bi}_2\text{Se}_3$  nanosheets under 808 nm laser. (c) Temperature elevation of the two  $\text{Bi}_2\text{Se}_3$  nanosheets for five laser on/off cycles.





is significantly higher than that of the Bi<sub>2</sub>Se<sub>3</sub>-80 nanosheets. It could be a result of lower scattering introduced by the smaller particles, by which the external light can be efficiently absorbed instead of being scattered.<sup>35</sup> Additionally, the thinner structure usually performs more violent atomic oscillation, which is beneficial to the photothermal conversion.

To further evaluate the photothermal stability of the two Bi<sub>2</sub>Se<sub>3</sub> nanosheets, time-dependent heating-cooling cycles under NIR laser were measured with 2 min laser heating and 10 min natural cooling (Fig. 4c). The cycles are repeated for five times and both of the two Bi<sub>2</sub>Se<sub>3</sub> nanosheets exhibit excellent photostability.

### 3.4. Photoacoustic performance

When nanoparticles absorb external light, their raised temperature will induce a transient thermoelastic expansion,<sup>36</sup> which could launch ultrasonic waves to form photoacoustic images.<sup>37</sup> As a result, the photoacoustic signal of the nanoparticles heavily depends on its optical absorption ability and photoacoustic conversion efficiency, which represents the efficiency of the conversion of absorbed optical energy to acoustic waves.<sup>38</sup> Therefore, with the same optical absorption, the material with higher photoacoustic conversion efficiency is able to perform stronger photoacoustic signal.<sup>39</sup>

Herein, the photoacoustic imaging is carried out to evaluate the photoacoustic conversion efficiency of the two Bi<sub>2</sub>Se<sub>3</sub> nanosheets. Fig. 5 exhibits the photoacoustic images of the two Bi<sub>2</sub>Se<sub>3</sub> nanosheets with same absorbance intensities of 0.3 at 808 nm. It is shown that the photoacoustic intensity of the Bi<sub>2</sub>Se<sub>3</sub>-30 nanosheets is 3 times higher than the Bi<sub>2</sub>Se<sub>3</sub>-80 nanosheets. Due to the smaller size of the Bi<sub>2</sub>Se<sub>3</sub>-30 nanosheets, the increased temperature introduces more cavities and further promotes the thermoelastic expansion. Therefore, the more effective photothermal conversion and greater thermal expansion synergistically will result in the higher photoacoustic conversion capability of the Bi<sub>2</sub>Se<sub>3</sub>-30 nanosheets.<sup>38</sup> Besides, the

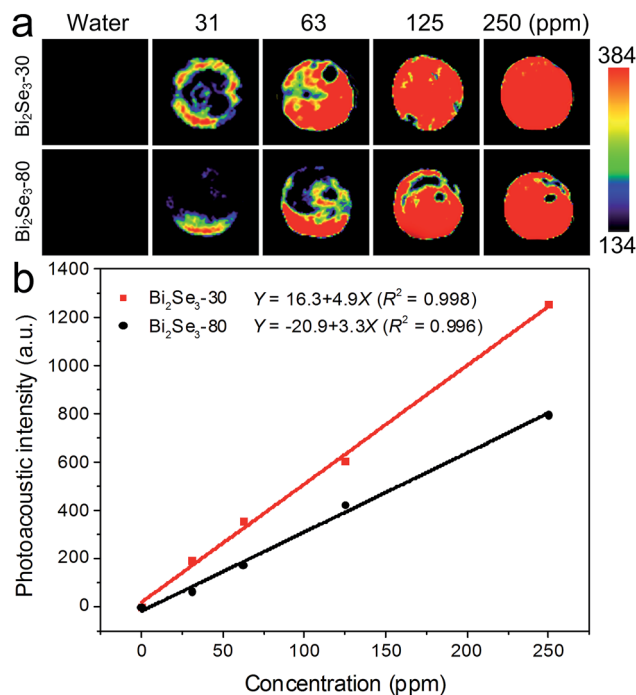


Fig. 6 (a) Photoacoustic images of the two Bi<sub>2</sub>Se<sub>3</sub> nanosheets aqueous solution with different concentrations. (b) Photoacoustic signal intensities as function of the concentrations.

photoacoustic signal intensities of the two Bi<sub>2</sub>Se<sub>3</sub> nanosheets are higher than that of GNRs, which is a commonly used photoacoustic agent (Fig. S4†).<sup>40</sup>

Subsequently, the photoacoustic images of the aqueous solutions of the two Bi<sub>2</sub>Se<sub>3</sub> nanosheets with concentrations from 0 to 250 ppm are illustrated in Fig. 6a. The concentration dependent intensities are described by the equations in Fig. 6b. The photoacoustic signals are enhanced with the increased Bi<sub>2</sub>Se<sub>3</sub> concentrations. The Bi<sub>2</sub>Se<sub>3</sub>-30 nanosheets show stronger photoacoustic signal than the Bi<sub>2</sub>Se<sub>3</sub>-80 nanosheets at all concentrations, confirming their better NIR photoacoustic performance.

## 4. Conclusions

In this study, we have successfully prepared two Bi<sub>2</sub>Se<sub>3</sub> nanosheets (Bi<sub>2</sub>Se<sub>3</sub>-30 and Bi<sub>2</sub>Se<sub>3</sub>-80) and characterized them utilizing TEM, HRTEM, XRD, EDS, AFM and UV-vis absorption spectroscopy. The results from optical absorption, NIR photothermal and photoacoustic effect demonstrate that both of the two Bi<sub>2</sub>Se<sub>3</sub> nanosheets present excellent optical performances. In particular, the optical performances of Bi<sub>2</sub>Se<sub>3</sub>-30 nanosheets with the smaller size are even better. These results indicate that the smaller Bi<sub>2</sub>Se<sub>3</sub> nanosheets are more promising for optical diagnostic and photothermal therapy.

## Conflicts of interest

There are no conflicts to declare.

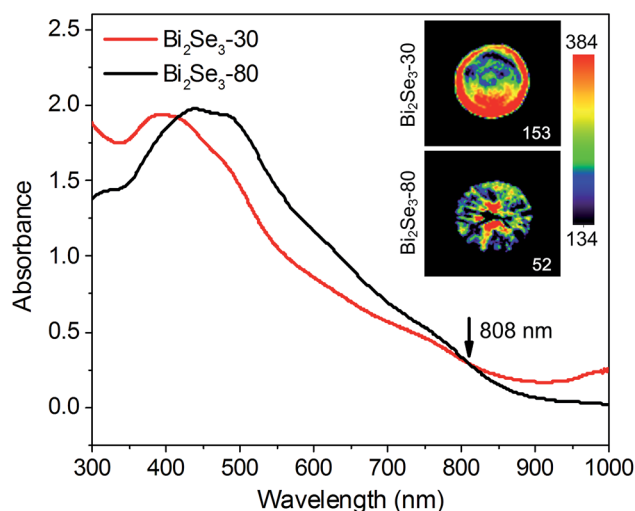


Fig. 5 Photoacoustic images of the two Bi<sub>2</sub>Se<sub>3</sub> nanosheets with the same absorbance intensities of 0.3 at 808 nm.



## Acknowledgements

This work was jointly supported by the National Natural Science Fund of China No. 51602204, Leading Talents of Guangdong Province Program (00201520), Guangdong Provincial Scientific Funds (2016A030313055), Program of Public Interest Research and Capability Construction of Guangdong Province (2015A020217010).

## Notes and references

- 1 J. Moore, *Nat. Phys.*, 2009, **5**, 378.
- 2 D. Kong and Y. Cui, *Nat. Chem.*, 2011, **3**, 845.
- 3 Y. Xia, D. Qian, D. Hsieh, L. Wray, A. Pal, H. Lin, A. Bansil, D. Grauer, Y. S. Hor, R. J. Cava and M. Z. Hasan, *Nat. Phys.*, 2009, **5**, 398.
- 4 H. Peng, K. Lai, D. Kong, S. Meister, Y. Chen, X. Qi, S. Zhang, Z. Shen and Y. Cui, *Nat. Mater.*, 2010, **9**, 225.
- 5 H. Zhang, C. X. Liu, X. L. Qi, X. Dai, Z. Fang and S. C. Zhang, *Nat. Phys.*, 2009, **5**, 438.
- 6 Y. Min, J. W. Roh, H. Yang, M. Park, S. Kim, S. Hwang, S. M. Lee, K. H. Lee and U. Jeong, *Adv. Mater.*, 2013, **25**, 1425.
- 7 Y. L. Chen, J. G. Analytis, J. H. Chu, Z. K. Liu, S.-K. Mo, X. L. Qi, H. J. Zhang, D. H. Lu, X. Dai, Z. Fang, S. C. Zhang, I. R. Fisher, Z. Hussain and Z.-X. Shen, *Science*, 2009, **325**, 178.
- 8 K. Kadel, L. Kumari, W. Z. Li, J. Y. Huang and P. P. Provencio, *Nanoscale Res. Lett.*, 2011, **6**, 57.
- 9 L. Sun, Z. Lin, J. Peng, J. Weng, Y. Huang and Z. Luo, *Sci. Rep.*, 2014, **4**, 4794.
- 10 L. Cheng, S. Shen, S. Shi, Y. Yi, X. Wang, G. Song, K. Yang, G. Liu, T. E. Barnhart, W. Cai and Z. Liu, *Adv. Funct. Mater.*, 2016, **26**, 2185.
- 11 J. Li, F. Jiang, B. Yang, X. R. Song, Y. Liu, H. H. Yang, D. R. Cao, W. R. Shi and G. N. Chen, *Sci. Rep.*, 2013, **3**, 1998.
- 12 Z. Li, Y. Hu, K. A. Howard, T. Jiang, X. Fan, Z. Miao, Y. Sun, F. Besenbacher and M. Yu, *ACS Nano*, 2016, **10**, 984.
- 13 X. D. Zhang, J. Chen, Y. Min, G. B. Park, X. Shen, S. S. Song, Y. M. Sun, H. Wang, W. Long, J. Xie, K. Gao, L. Zhang, S. Fan, F. Fan and U. Jeong, *Adv. Funct. Mater.*, 2014, **24**, 1718.
- 14 B. L. Li, M. I. Setyawati, L. Chen, J. Xie, K. Ariga, C. T. Lim, S. Garaj and D. T. Leong, *ACS Appl. Mater. Interfaces*, 2017, **9**, 15286.
- 15 Y. Zhang, K. He, C. Z. Chang, C. L. Song, L. L. Wang, X. Chen, J. F. Jia, Z. Fang, X. Dai, W. Y. Shan, S. Q. Shen, Q. Niu, X. L. Qi, S. C. Zhang, X. C. Ma and Q. K. Xue, *Nat. Phys.*, 2010, **6**, 584.
- 16 J. Zhang, Z. Peng, A. Son, Y. Zhao, Y. Xiong, B. Peng, J. Wang, M. S. Dresselhaus and Q. Xiong, *Nano Lett.*, 2011, **11**, 2407.
- 17 Z. Li, S. Tang, B. Wang, Y. Li, H. Huang, H. Wang, P. Li, C. Li, P. K. Chu and X. F. Yu, *ACS Biomater. Sci. Eng.*, 2016, **2**, 789.
- 18 C. H. J. Choia, J. E. Zuckerman, P. Webster and M. E. Davis, *Proc. Natl. Acad. Sci. U. S. A.*, 2011, **108**, 6656.
- 19 Y. Min, G. D. Moon, B. S. Kim, B. Lim, J. S. Kim, C. Y. Kang and U. Jeong, *J. Am. Chem. Soc.*, 2012, **134**, 2872.
- 20 H. Xie, Z. Li, Z. Sun, J. Shao, X. F. Yu, Z. Guo, J. Wang, Q. Xiao, H. Wang, Q. Q. Wang, H. Zhang and P. K. Chu, *Small*, 2016, **12**, 4136.
- 21 Z. Li, J. Shao, Q. Luo, X. F. Yu, H. Xie, H. Fu, S. Tang, H. Wang, G. Han and P. K. Chu, *Biomaterials*, 2017, **133**, 37.
- 22 A. Zhuang, J. J. Li, Y. C. Wang, X. Wen, Y. Lin, B. Xiang, X. Wang and J. Zeng, *Angew. Chem.*, 2014, **126**, 6543.
- 23 S. Cho, N. P. Butch, J. Paglione and M. S. Fuhrer, *Nano Lett.*, 2011, **11**, 1925.
- 24 X. Liu, J. Xu, Z. Fang, L. Lin, Y. Qian, Y. Wang, C. Ye, C. Ma and J. Zeng, *Nano Res.*, 2015, **8**, 3612.
- 25 Z. Sun, S. Liufu, X. Chen and L. Chen, *Chem. Commun.*, 2010, **46**, 3101.
- 26 J. T. Robinson, S. M. Tabakman, Y. Liang, H. Wang, H. S. Casalongue, D. Vinh and H. Dai, *J. Am. Chem. Soc.*, 2011, **133**, 6825.
- 27 Y. Yi, X. F. Yu, W. Zhou, J. Wang and P. K. Chu, *Mater. Sci. Eng., R*, 2017, **120**, 1.
- 28 Z. Sun, H. Xie, S. Tang, X. F. Yu, Z. Guo, J. Shao, H. Zhang, H. Huang, H. Wang and P. K. Chu, *Angew. Chem.*, 2015, **127**, 11688.
- 29 L. Sun, Z. Lin, J. Peng, J. Weng, Y. Huang and Z. Luo, *Sci. Rep.*, 2014, **4**, 4794.
- 30 X. Yang, X. Wang and Z. Zhang, *J. Cryst. Growth*, 2005, **276**, 566.
- 31 S. Subramanian and P. Padiyan, *Mater. Chem. Phys.*, 2008, **107**, 392.
- 32 Q. Tian, F. Jiang, R. Zou, Q. Liu, Z. Chen, M. Zhu, S. Yang, J. Wang, J. Wang and J. Hu, *ACS Nano*, 2011, **5**, 9761.
- 33 J. Cui, R. Jiang, S. Xu, G. Hu and L. Wang, *Small*, 2015, **11**, 4183.
- 34 P. Huang, J. Lin, W. Li, P. Rong, Z. Wang, S. Wang, X. Wang, X. Sun, M. Aronova, G. Niu, R. D. Leapman, Z. Nie and X. Chen, *Angew. Chem.*, 2013, **125**, 14208.
- 35 C. M. Hessel, V. P. Pattani, M. Rasch, M. G. Panthani, B. Koo, J. W. Tunnell and B. A. Korgel, *Nano Lett.*, 2011, **11**, 2560.
- 36 L. Cavigli, M. Angelis, F. Ratto, P. Matteini, F. Rossi, S. Centi, F. Fusi and R. Pini, *J. Phys. Chem. C*, 2014, **118**, 16140.
- 37 L. V. Wang and S. Hu, *Science*, 2012, **335**, 1458.
- 38 Y. Shi, H. Qin, S. Yang and D. Xing, *Nano Res.*, 2016, **9**, 3644.
- 39 Y. S. Chen, W. Frey, S. Kim, P. Kruizinga, K. Homan and S. Emelianov, *Nano Lett.*, 2011, **11**, 348.
- 40 E. C. Cho, C. Kim, F. Zhou, C. M. Cobley, K. H. Song, J. Chen, Z. Y. Li, L. V. Wang and Y. Xia, *J. Phys. Chem. C*, 2009, **113**, 9023.

